WILEY-VCH

RESEARCH ARTICLE

Integrated Soft Porosity and Electrical Properties of Conductive-on-Insulating Metal-Organic Framework Nanocrystals

Ming-Shui Yao,[a, b, f] Ken-ichi Otake,* [a] Jiajia Zheng,[a] Masahiko Tsujimoto,[a] Yi-Fan Gu,[a,c] Lu Zheng,[a,c] Ping Wang,[a] Shivanna Mohana,[a] Mickaele Bonneau,[a] Tomoyuki Koganezawa,[d] Tetsuo Honma,[d] Hirotaka Ashitani,[e] Shogo Kawaguchi,[d] Yoshiki Kubota,[e, g] and Susumu Kitagawa*[a]

[a] Prof. M. S. Yao, Prof. K. Otake, M. Tsujimoto, Dr. Y. F. Gu, L. Zheng, Dr. P. Wang, Dr. S. Mohana, Dr. M. Bonneau, Prof. S. Kitagawa
Institute for Integrated Cell-Material Sciences, Kyoto University, Institute for Advanced Study, Kyoto University
Yoshida, Ushinomiya-cho, Sakyo-ku, Kyoto 606-8501(Japan)
E-mail: otake.kenichi.8a@kyoto-u.ac.jp; kitagawa@icems.kyoto-u.ac.jp

[b] Prof. M. S. Yao
State Key Laboratory of Multi-phase Complex Systems, Institute of Process Engineering, Chinese Academy of Sciences
Zhongguancun Beiertiao No. 1, Haidian District, Beijing, 100190 (China)

[c] Dr. Y. F. Gu, L. Zheng
College of Environmental Science and Engineering, State Key Laboratory of Pollution Control and Resource Reuse, Tongji University
Siping Road 1239, Shanghai 200092 (China)

[d] T. Koganezawa, T. Honma, S. Kawaguchi
Japan Synchrotron Radiation Research Institute (JASRI),
1-1-1, Kouto, Sayo-cho, Sayo-gun, Hyogo 679-5198 (Japan)

[e] H. Ashitani, Prof. Y. Kubota
Department of Physical Science, Graduate School of Science, Osaka Prefecture University, Osaka (Japan)

[f] Prof. M. S. Yao
Center of Materials Science and Optoelectronics Engineering, University of Chinese Academy of Sciences, Chinese Academy of Sciences
No.19(A) Yuquan Road, Shijingshan District, Beijing, 100049 (China)

[g] Prof. Y. Kubota
Department of Physics, Graduate School of Science, Osaka Metropolitan University, Osaka (Japan)

Supporting information for this article is given via a link at the end of the document.

Abstract: A one-stone, two-bird method to integrate the soft porosity and electrical properties of distinct metal-organic frameworks (MOFs) into a single material involves the design of conductive-on-insulating MOF (*c*MOF-on-*i*MOF) heterostructures that allow for direct electrical control. Herein, we report the synthesis of *c*MOF-on-*i*MOF heterostructures using a seeded layer-by-layer method, in which the sorptive *i*MOF core is combined with chemiresistive *c*MOF shells. The resulting *c*MOF-on-*i*MOF heterostructures exhibit enhanced selective sorption of CO_2 compared to the pristine *i*MOF (298 K, 1 bar, $S_{CO2/H2}$ from 15.4 of ZIF-7 to 43.2–152.8). This enhancement is attributed to the porous interface formed by the hybridization of both frameworks at the molecular level. Furthermore, owing to the flexible structure of the *i*MOF core, the *c*MOF-on-*i*MOF heterostructures with semiconductive soft porous interfaces demonstrated high flexibility in sensing and electrical "shape memory" toward acetone and CO_2. This behavior was observed through the guest-induced structural changes of the *i*MOF core, as revealed by the *operando* synchrotron grazing incidence wide-angle X-ray scattering measurements.

Introduction

Metal-organic frameworks (MOFs) or porous coordination polymers (PCPs) are an emerging class of crystalline porous materials constructed by coordinating metal nodes with organic linkers.[1] Unlike conventional porous materials, such as zeolites or porous carbons, some MOFs exhibit soft porosity arising from their lattice flexibility. The concept of soft porosity in MOFs has garnered significant attention owing to its potential to switch functionalities.[2] Numerous studies have been conducted to understand the mechanisms underlying their flexibility, and several theoretical investigations have even suggested the possibility of electrically controlling their structural flexibility.[3] However, achieving electrical control over the structural functionalities of MOFs is challenging because most MOFs exhibit limited electrical conduction properties (referred to as insulating MOFs, or *i*MOFs).[4] One pioneering example is the indirect electrical control (via *E*-field polarization) of a MOF membrane to enhance its molecular sieving capability by approximately 1 h.[5] To realize the direct electrical control, which has yet to be implemented, a promising approach involves molecular-level integration of *i*MOFs and electronically conductive MOFs (*c*MOFs). These hybrid materials, known as MOF-on-MOF hybrids or so-called fourth-generation MOFs, are expected to simultaneously or alternately exhibit multiple functions when combined.[6] Therefore, we anticipate that exploring a general method for preparing *c*MOF-on-*i*MOF heterostructures would be an effective one-stone, two-bird method for integrating the soft porosity and conductivity of distinct MOFs into a single material.[6b, 6d, 7]

One major obstacle in combining two distinct MOFs is the difficulty of modulating the transition interfaces at the molecular level owing to their lattice mismatch.[6c, 8] Thus far, numerous strategies for synthesizing various MOF-on-MOF heterostructures have been developed.[6b-d, 7-9] However, most of these methods involve the combination of *i*MOFs (*i*MOF-on-*i*MOF), with the exception being a van der Waals *i*MOF-on-*c*MOF thin-film, which requires well-defined two-dimensional (2D) nanosheets of *i*MOFs for effective transfer onto the *c*MOF thin film.[6c] Devising a general method to precisely control the growth of the secondary *c*MOFs on different *i*MOFs remains highly challenging owing to a significant lattice mismatch and different topologies. The lattice mismatch hinders

the formation of one-to-one coordination bonds at the interface, which are crucial for the nucleation and growth of the secondary MOFs.

Herein, we report the controlled synthesis of a series of *c*MOF-on-*i*MOF core-shell/sheath heterostructures using a seeded layer-by-layer (LbL) liquid phase epitaxial (LPE) growth method.[10] We utilized the flexible 3D sodalite (SOD)-topology [Zn(bim)$_2$] (also known as MAF-3 or ZIF-7, bim = benzimidazole) nanocrystals (ncs)[11] for the sorptive *i*MOF core to induce the reversible guest-responsive structural changes. For the conductive *c*MOF shell, we selected 2D π-conjugated *c*MOFs, specifically Cu-HHTP (HHTP = 2,3,6,7,10,11 – hexahydrotriphenylene) and Cu-HITP (HITP = 2,3,6,7,10,11– hexaiminotriphenylene), owing to their highly redox-active ligands, satisfactory conductivity (0.02-0.2 S cm^{-1},[12] measured using two probe method with pelletized sample), and facile LbL growth at low temperatures. Our goal extends beyond simple adsorption and sensing applications. We employ gas molecules as probes to explore the fundamental scientific issues related to integrating nanocrystals with soft porosity and electrical properties, as well as the resulting novel electrical functionalities arising from their softness. The enhanced gate-type selective sorption of CO_2, even without electrical control, confirms the existence of a porous interface resulting from the molecular-level hybridization of both materials. Under direct electrical control and the transduced electrical signals, the *c*MOF-on-*i*MOF heterostructures with the semiconductive soft porous interfaces exhibit visible flexibility and electrical "shape memory" effects.[13]

Results and Discussion

We synthesized *c*MOF-on-*i*MOF heterostructures by combining ZIF-7 ncs as the *i*MOF core and Cu-HXTP (X= H or I) thin films as the *c*MOF shells using the LbL LPE method. Despite significant lattice mismatch and different topologies, the presence of rich defects and dynamic states on the surface of *i*MOF in liquid solvents provide potential chemical bonding sites for the *c*MOF.[14] Inspired by this concept, we first formed an intermediate layer by treating ZIF-7 ncs with a shell-ligand-exchange-reaction (SLER[15]) in an ethanolic solution containing HHTP/HITP ligands and N-methyl pyrrolidone (NMP) at 65°C (**Figure 1a**, for a detailed procedure, refer to the Methods section).

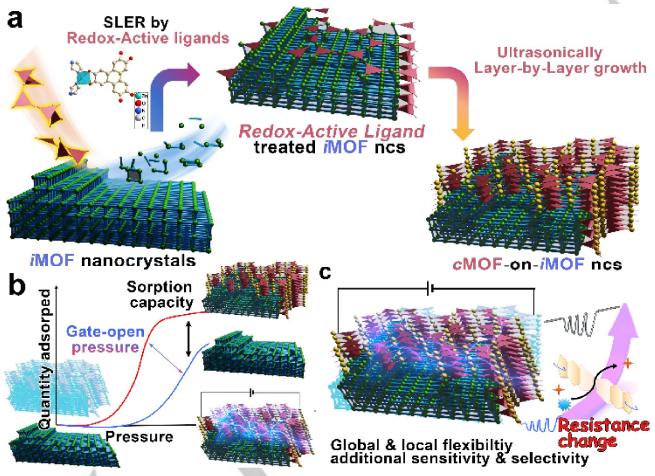

Figure 1. Design of the heterostructures and structure-function relationships. (a) Schematic of the ultrasonically LbL LPE preparation of *c*MOF-on-*i*MOF heterostructured nanocrystals (ncs), and the corresponding (b) responsive gas/vapor adsorption with/without electrical control, and (c) electrically-transduced soft porosity related chemiresistive gas/vapor sensing.

Typically, MOFs with large lattice structures are more likely to grow on the crystal surfaces of MOFs with smaller lattice structures because the latter provides a relatively high density of coordination sites for the former. The formation of an intermediate layer and the larger lattice of the *c*MOF contributed to their growth on *i*MOFs, despite the significant lattice mismatch and topology differences. Furthermore, the bulky size of HHTP/HITP ligands (~ 0.97 nm) prevented the undesired loading into the channels of *i*MOF cores. Subsequently, Cu-HHTP/Cu-HITP frameworks were prepared on the HHTP/HITP ligand-treated *i*MOF crystals using an ultrasonically assisted LbL LPE method. A *c*MOF shell/sheath with varying thicknesses was obtained by adjusting the number of growth cycles, denoted as *i*MOF@*c*MOF-*x*C (*x* represents the number of growth cycles at a concentration of 15.0 mg mL^{-1}, for further details see SI) or *i*MOF@*c*MOF-s-xC (at a concentration of 3.0 mg mL^{-1}).

Transmission electron microscopy (TEM) images of various *i*MOF@Cu-HHTP-xC samples demonstrate that the morphology and crystal size of the *i*MOF ncs remained unchanged after depositing thin layers of *c*MOF (**Figure S1, SI**). The

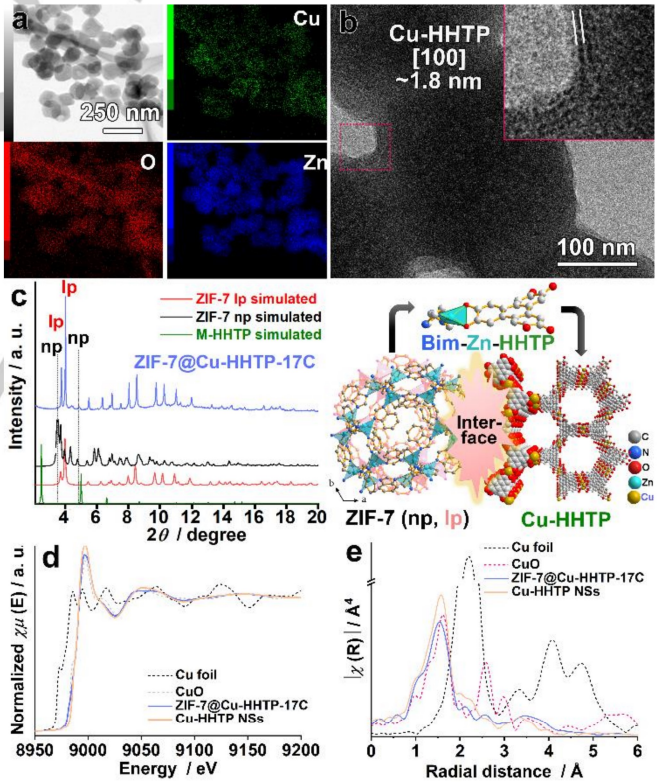

Figure 2. TEM, PXRD, XANES and EXAFS of ZIF-7@Cu-HHTP-17C ncs. (a) The TEM image of ZIF-7@Cu-HHTP-17C ncs (followed by the corresponding EDS mapping images of Cu, O, and Zn). (b) Cu-HHTP sheath of ZIF-7@Cu-HHTP-17C showing (100) face (the inset is the enlarged image of the red zone), (c) the synchrotron PXRD patterns of ZIF-7@Cu-HHTP-17C compared with simulated ZIF-7, Cu-HHTP and possible hybrid bonds. Data were collected at beamline 02B2 in SPring 8, Japan (λ=0.79962 Å), (d) Cu K-edge XANES spectra. Data were collected at beamline BL11S2 in the Aichi Synchrotron Radiation Center, Japan; and (e) Fourier transform EXAFS of Cu foil, CuO, Cu-HHTP, ZIF-7@Cu-HHTP-xC (x=10, 17), and ZIF-7@Cu-HITP-5C.

corresponding energy-dispersive X-ray spectroscopy (EDX) mapping images of Cu, Zn, C, and N confirm the core-shell heterostructure of ZIF-7@Cu-HHTP ncs (**Figures 2a** and **S1**). Moreover, the high-resolution TEM image of the ZIF-7@Cu-HHTP-17C ncs clearly reveals a rough Cu-HHTP shell layer with a thickness of a few nanometers and a well-defined lattice image of the (110) face of the ZIF-7 core (**Figure S1d**, with a lattice mismatch of approximately 5.7% along *a/b* and 18.0% along *c*). Additionally, lattice images of the (100) face of the Cu-HHTP sheath occur on some particle edges (**Figure 2b**). Although only with seven cycles of *c*MOF growth processes were performed, ZIF-7@Cu-HHTP-s-7C ncs exhibited rough surfaces and a substantial Cu-MOF shell owing to the five-fold feeding of Cu and HHTP solutions to ZIF-7 ncs during the process (**Figure S2**). Similarly, the EDX mapping images display distinguishable Zn-Cu core-shells. Weak lattice images of the (100) face of Cu-HHTP/Cu/HITP sheathes are also observed for ZIF-7@Cu-HHTP-s-7C, ZIF-7@Cu-HITP-5C, and ZIF-7@Cu-HITP-s-5C (**Figures S2** and **S3**).

The synchrotron powder X-ray diffraction (PXRD) patterns of various ZIF-7@Cu-HHTP-xC (x=5, 10, 17, 25), ZIF-7@HHTP (ZIF-7 after SLER with HHTP), ZIF-7@Cu-HHTP-s-xC (x=2, 4, 7), and ZIF-7@Cu-HITP-5C reveal the coexistence of the narrow-pore (np) and large-pore (lp) phases of ZIF-7. This coexistence depends on the degree of guest molecule occupation within the framework (**Figures 2c** and **S4-S8**). However, no peaks corresponding to hexagonal Cu-HHTP appear because of the lower ratio and relatively low crystallinity of *c*MOF shells compared to the ZIF-7 ncs core. To clarify the chemical state of the Cu species in the *c*MOF shells, X-ray absorption near-edge structure (XANES) and extended X-ray absorption fine structure (EXAFS) analyses were performed. The Cu K-edge XANES spectra show that both ZIF-7@Cu-HHTP-xC (x=10, 17) and ZIF-7@Cu-HITP-5C show a typical Cu(II) peak above ~8985 eV (**Figures 2d** and **S9a**), which is similar to that of the reference Cu-HHTP/Cu-HITP and CuO. The radial structure functions of ZIF-7@*c*MOFs clearly demonstrate the characteristic Cu-O/Cu-N coordination in Cu-HHTP/Cu-HITP with an intensive peak at approximately 1.53/1.56 Å (**Figures 2e** and **S9b**), which is similar to that observed in crystalline Cu-HHTP/Cu-HITP (~1.56 Å). The absence of distinct structural peaks and the diminishment of the signal at ~2.21 Å indicate that no heavy backscattering atoms (Cu) are bound to the Cu sites in the Cu-HHTP shells. Consequently, the XANES and EXAFS spectra of the ZIF-7@*c*MOFs, along with the results of contrasting experiments, provide robust evidence for the presence of the square planar building units of CuO_x/CuN_x, supporting the Cu-HHTP/Cu-HITP structures of the *c*MOF shells. Moreover, the coordination bonds of Cu-HHTP are also confirmed by the absence of infrared (IR) spectroscopy peaks corresponding to free –OH groups and the appearance of new peaks assigned to the square planar building units of Cu-HHTP (**Figure S10**). The corresponding elemental analysis (EA) results for ZIF-7@HHTP, ZIF-7@Cu-HHTP-10C, and ZIF-7@Cu-HHTP-17C further demonstrate the composite nature of their structures and are consistent with the results obtained from their related thermogravimetric analysis (TG/DTA) (**Figure S11** and **Table S1-S3**, for additional details refer to SI).

To evaluate porous properties, such as the sorption capacity and gate-opening behavior, which provide structural information about the interface layer and respective MOFs, we conducted CO_2 sorption isotherm measurements. Interestingly, ZIF-7@Cu-HHTP-xC and ZIF-7@Cu-HITP-xC not only exhibit enhanced sorption capacity toward CO_2, accompanied by the one-stage (273 K and 298 K) or two-stage (195 K) gate-opening behaviors,[16] but also demonstrate reduced gate-opening pressure (p_{go}) (**Figures 3a** and **S12-15**). The *in situ* PXRD patterns measured under varying CO_2 pressures (195 K) of ZIF-7@Cu-HITP-5C reveal a reversible two-step phase transition

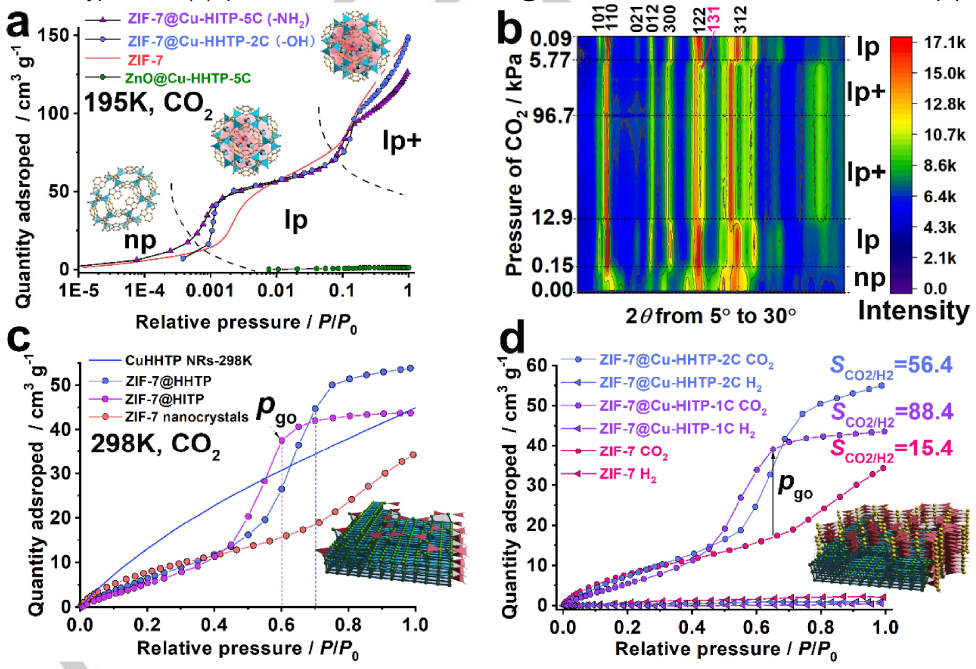

Figure 3. The modulated soft porosity without electrical control. (a) CO_2 sorption isotherm at 195 K of ZIF-7@*c*MOFs compared with bare ZIF-7 ncs; (b) The contour plot for the *in situ* PXRD patterns of ZIF-7@Cu-HITP-5C upon exposure to CO_2 with varying pressure; (c) CO_2 sorption isotherm of Cu-HHTP NRs, ZIF-7 ncs, and ligand treated ZIF-7 ncs (ligand=HITP, HHTP) at 298 K; (d) CO_2/H_2 selectivity comparison of ZIF-7 and ZIF-7@*c*MOFs at 298 K.

among the guest-free ZIF-7(np), ZIF-7(lp) and ZIF-7 (lp+; ordered rearrangement of CO_2,[16b] **Figure 3b**). The np-lp transition took place at approximately 0.10-0.15 kPa (~2.0-2.5 mmol g^{-1}, where the number of CO_2 molecules adsorbed in one ZIF-7 unit cell (N_{CO2}) =11.0-13.8), which is ~0.3 kPa for pure ZIF-7 ncs, and the lp-lp+ transition took place at around 10-15 kPa (saturated at ~5.6-6.7 mmol g^{-1}, with N_{CO2} = 30.8-37.0).[16b] These results imply that the *c*MOF shells facilitate the gate-opening behavior of ZIF-7 core toward CO_2, although they are not the main components of ZIF-7@*c*MOFs (<10 mol.%, **Table S1-S3**). Assuming that no molecular-level hybridization occurs at the interface, the estimated CO_2 sorption behavior of ZIF-7@Cu-HHTP, calculated based on the corresponding components alone, closely resembles that of ZIF-7. Even with 50 wt.% of Cu-HHTP, only a slight enhancement in adsorption without promoting gate-opening behaviors is observed (**Figure S16**). This emphasizes the essential role of the porous interface frameworks formed by Zn-bim, Cu-HHTP, and possible hybrid bonds that occur at the molecular level.

To investigate the origin of the CO_2 sorption enhancement in cMOF-on-ZIF-7 ncs, we examined the influence of modifying the outer surface of the ZIF-7 ncs core. As previously reported, ZIF-7 ncs (size, ~100 nm) are more flexible than pure ZIF-7 microcrystals (size, ~100-200 μm) because of their defective outer surface.[16b] Consequently, the ZIF-7 ncs adsorb slightly higher amounts of CO_2 molecules at lower pressures before gate opening (273 K and 298 K, **Figures 3c, S17,** and **S18**). Furthermore, the np-lp phase transition curves of ZIF-7 ncs also exhibit a more gradual slope at higher pressure, indicating a higher energy barrier (the Gibbs energy change, $\Delta G^{\ddagger}_2$, red) compared to single crystals ($\Delta G^{\ddagger}_1$, black) resulting from the defective outer surface (the energy difference between np and lp is ΔG_1=ΔG_2=29.9 kJ mol^{-1} for one-unit cell according to density functional theory (DFT) calculations[16a], see Figure S19, SI for details). This energy barrier is expected to be adjustable by modifying the outer surface environment through an exchange with a foreign organic ligand during the SLER process (**Figure S19**). However, creating such an interface may introduce instability in the np state, leading to a decrease in gate pressure. Consequently, at the np-lp transition stage for CO_2 at different temperatures, reduced p_{go} and enhanced sorption are observed (**Figures 3c** and **S20**). Controlling the redox activity of the shell by adding redox-active Cu ions and the foreign organic ligands to form a Cu-based MOF shell effectively modulates both the sorption capacity and p_{go} (**Figures S21-S23**). These findings correlate well with the heat of adsorption (Q_{st}) values of the corresponding shell MOFs (**Figure S24**). Therefore, it can be concluded that the high CO_2 affinity of the redox-active *c*MOF shells and the porous hybridized interfaces not only act as a "pump" to lower the energy barrier between the two phases ($\Delta G^{\ddagger}_2$, gradient color, **Figure S19**), thus triggering the gate-opening of the ZIF-7 core at relatively low pressure. Furthermore, the sorption capacity is enhanced by facilitating the fully open phase of ZIF-7 (lp) phase and enabling additional adsorption on the interface and *c*MOF shells. Moreover, the effect of the *c*MOF shell on ZIF-7 results in a smaller gate-closing pressure for CO_2 (~20 kPa) compared to pure ZIF-7 ncs at 298 K (~40 kPa, **Figure S23**), further supporting the enhancement of CO_2 affinity.

To assess the guest selectivity of the *c*MOF-on-*i*MOF, sorption experiments using other gas (H_2, CH_4, and O_2) and vapors (acetone and toluene) were performed (**Figure S25** and **Table S4**). Because both ZIF-7 and *c*MOFs have limited adsorption capacities for H_2 and CH_4, *c*MOF-on-*i*MOF does not exhibit significant adsorption for these gases. Hence, the reduced p_{go} and enhanced sorption capacity toward CO_2 can be effectively utilized to improve the sorption selectivity of CO_2 over H_2/CH_4 (at 1 bar, for ZIF-7 $S_{CO2/H2}$ increases from 15.4 to 43.2-152.8, and for ZIF-7 $S_{CO2/CH4}$ increases from 7.6 to 8.3-38.5), along with a broader working pressure range at 298 K (**Figure 3d, Table S4**). Furthermore, the intrinsic stability in the presence of air and humidity, combined with a low activation temperature, indicates *c*MOF-on-*i*MOF's promising potential for gas separation applications. Additionally, as observed from the adsorption curves (**Figure S25**), low concentrations of gas molecules both before (*e.g.*, acetone, 100 ppm, 10^{-4}) and after (*e.g.*, acetone, 1000 ppm, 10^{-3}) the gate opening of ZIF-7, representing the narrow and large channels of ZIF-7 (np) and lp, respectively, significantly affect their diffusion and adsorption in the composite frameworks. Theoretical calculations indicate that acetone interacts more strongly with ZIF-7 than with CO_2. This is because the difference in polarizability of acetone and CO_2 determines the noncovalent interactions between the guest molecules and the host frameworks (**Figures 4a** and **4b**). Therefore, the electrical properties of the *c*MOF can be controlled by combining the electrical properties of the *c*MOF with the gate-opening behavior of the ZIF-7 core.

The semiconductive nature of the *c*MOF sheath allows the fabrication of the chemiresistive sensors based on *c*MOF-on-*i*MOF materials, which are effective for monitoring the diffusion and adsorption of gas molecules at the ppm level through the transduction of electrical signals.[4d, 17] Encouraged by the enhanced capacity and selectivity of the obtained *c*MOF-on-*i*MOF, the real-time detection of gas/vapor was conducted using chemiresistors based on *c*MOF-on-*i*MOFs (see SI for details).[6c, 18] The chemiresistive properties and conductivity were confirmed using NH_3 vapor, exhibiting reversible and high responses (100 ppm, $R_{average}$ = 215.5%, the average value of the responses toward NH_3 for five successive cycles for ZIF-7@Cu-HHTP-17C, **Figures S26** and **S27**). The sensor showed fast response times concentration-dependent responses with good linearity, and temperature-dependent sensor conductivity on a logarithmic scale (**Figures S28** and **S29**).

Unlike NH_3, the *i*MOF core of ZIF-7 exhibits gate-opening behavior toward acetone vapor with a p_{go} threshold of approximately 1000 ppm. The interface formed through molecular-level hybridization between the ZIF-7 and Cu-HHTP frameworks enables a sensitive change in the conductivity of *c*MOF shells, corresponding to the structural deformation of the *i*MOF cores (**Figure S30**), resulting from the changes in the interconnections of *c*MOF domain interparticles or intraparticles. Consequently, increasing the concentration of acetone results in a sharp increase in the response of the ZIF-7@Cu-HHTP chemiresistive sensors, ranging from 1000 to 1132 ppm (**Figures 4c** and **S30-32**). In contrast, without the hybridization, the response of the pristine *c*MOF exhibits low and linear log-log plots of response *vs.* concentration (**Figures 4c** and **S33**).

Furthermore, gate opening under a high acetone results in a metastable electrical state (*E*-meta) with incomplete desorption of acetone from the frameworks. Consequently, all ZIF-7@Cu-HHTP sensors exhibit significant gate-opening behavior at low acetone concentration levels during the second cycle (100-500 ppm, **Figures 4c** and **S34-36**). In addition, structural deformation

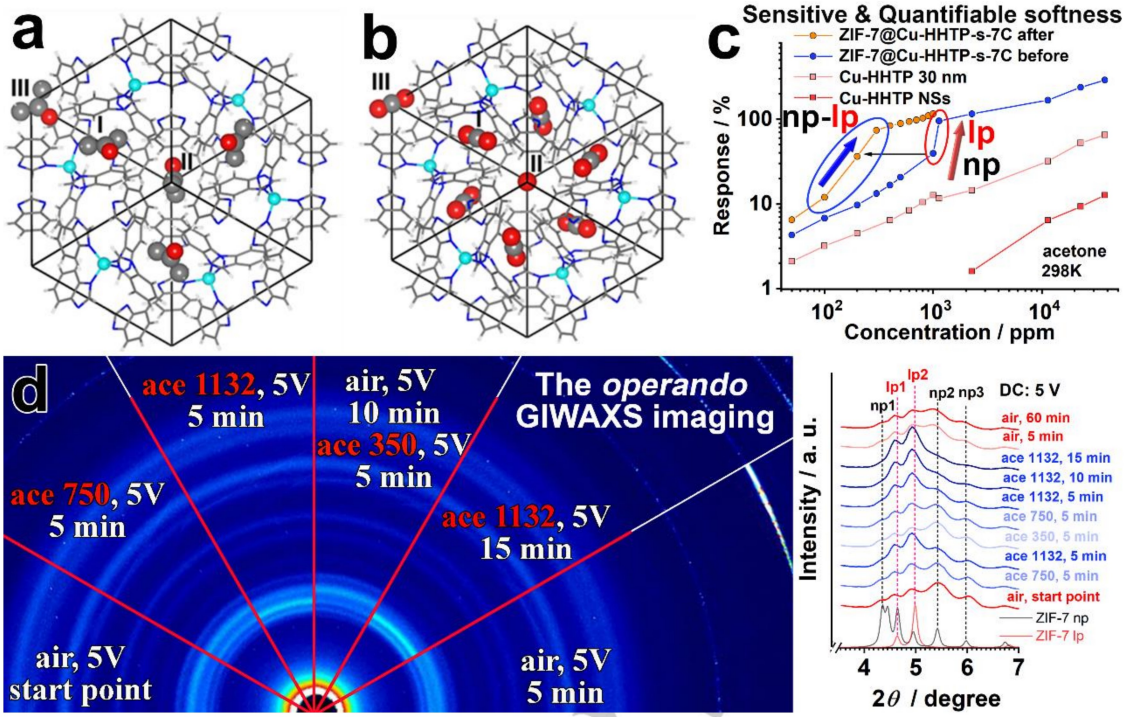

Figure 4. Integrated soft porosity and electrical properties for electrical gating and "shape memory." Adsorption positions for (a) acetone and (b) CO_2 in ZIF-7, revealed by Monte-Carlo simulations followed by density functional theory calculations. There are three sites for the adsorption of both acetone and CO_2. Because of the difference in molecular size between acetone and CO_2, site I has three symmetrical positions for acetone adsorption but six symmetrical positions for CO_2 adsorption. For sites II and III, there is only one position for both acetone and CO_2 adsorptions. Therefore, the maximum numbers of adsorbed guest molecules in ZIF-7 are 5 for acetone and 8 for CO_2 adsorptions, respectively. (c) The log-log plots of the chemiresistive response versus the concentration of pure *c*MOFs and ZIF-7@Cu-HHTP-s-7C (before and after gate opening) gas sensors toward acetone vapor; (d) the GIWAXS patterns and the converted patterns of ZIF-7@Cu-HHTP-s-7C during electrically-transduced sensing process, data were collected at beamline 46XU in SPring 8, Japan (λ=1.0 Å).

of the flexible core results in an additional resistance change, enhancing the responses. This implies that ZIF-7@*c*MOF forms a distinct metastable phase compared to the pristine *c*MOF sensor, referred to as electrical "shape memory."

To investigate the underlying mechanism of the enhanced chemiresistive responses and electrical "shape memory" effects of *c*MOF-on-*i*MOF under the actual working conditions (chemiresistive sensing process), we performed the synchrotron grazing incidence wide-angle X-ray scattering (GIWAXS) measurements in *operando* (the *Latin gerund*, which means working or operating[19]) while controlling the gas atmosphere and applying a voltage (**Figures 4d, S37** and **S38**).

Upon exposure to acetone, the GIWAXS *operando* images and the corresponding converted patterns shown in **Figure 4d** clearly confirm the np-lp transition of ZIF-7@Cu-HHTP-s-7C after 5 min of exposure (~1132 ppm). The structural changes induced by the guest molecules are further confirmed by a rapid phase transition from lp back to np upon exposure to air, resulting in a narrow phase with five typical weak peaks between 4-6°. Furthermore, increasing the exposure time to 15 min (~1132 ppm of acetone) allows for complete gas diffusion through the film and structural deformation of the ZIF-7 cores. This results in a fully open ZIF-7(lp) phase with two distinctive strong peaks at (101) and (110) between 4-6° that are clearly distinguishable from ZIF-7(np). The GIWAXS phase transition results are well consistent with the observed time-dependent response-recovery curve (**Figure S39**). Following air purging, a metastable state containing a mixture of mainly np and a few lp phases was identified as the origin of the electrical "shape memory" effect, consistent with the subsequently observed reduced p_{go} of acetone (~500 ppm, **Figure 4c**).

Notably, when the gas probe is changed to the sensing-inactive CO_2, electrical on/off gating is caused by the "shape memory" effect. Without the presence of the metastable phase, CO_2 is effectively captured by *c*MOF shells under electrical control (*i.e.*, electrical gating off), and the *i*MOF cores remain in the gate-closed state (① **Figure 5**), failing to trigger gate-type responses (Route A in **Figures 5, S40a** and **S41**). The *operando* GIWAXS results for ZIF-7@*c*MOF initially showed a sluggish np-lp transition in response to CO_2 (**Figure S42**), consistent with the chemiresistive sensing results. This implies that the CO_2-induced lp phase only occurs in a small area near the interface because of the blocking effect of the *c*MOF shells, thus failing to trigger gate-open state of the ZIF-7 core (② **Figure 5**). However, for ZIF-7@*c*MOF with a metastable state (③ **Figure 5**), the electrical gating off mode is triggered by "shape memory" effects, resulting in a gate-type behavior (type IV) characterized by significantly enhanced responses (~one order of magnitude) and faster

response speeds (from over 4 min to less than 1 min, Route B in **Figures 5, S40b** and **S43-S47**). The electrical "shape memory" eliminates the capture effects of *c*MOF shells under electrical control (electrical gating off, **Figure S41**) and accelerates the phase transition at concentrations below p_{go}. This is confirmed by the CO_2 sorption isotherm at 273 K.

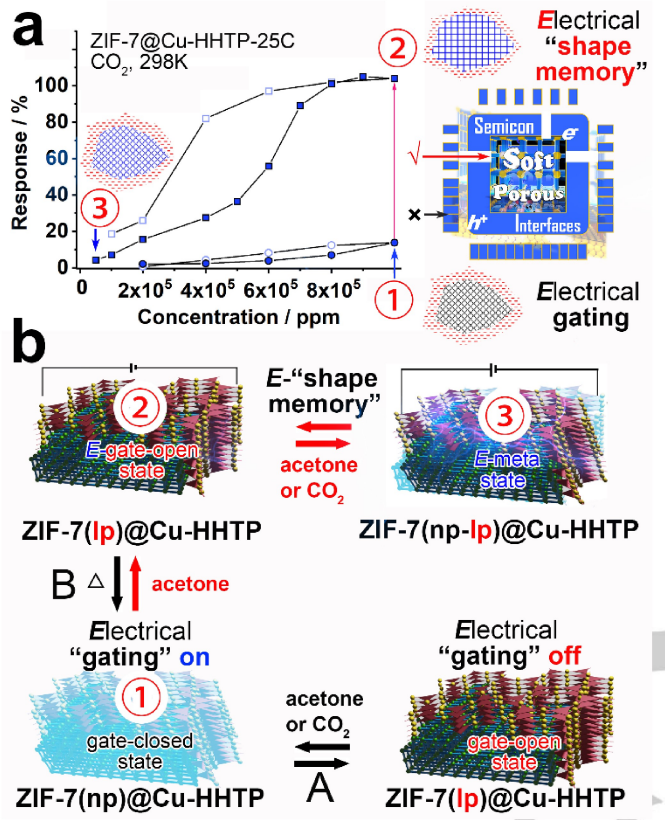

Figure 5. Integrated soft porosity and electrical properties for electrical gating and "shape memory." (a) The chemiresistive responses of ZIF-7@Cu-HHTP-25C sensors toward CO_2 before (circle) and after (square) the shape memory; (b) schematic illustration of (Route A) directly from the gate-close state (①) to gate-open state without electrical "gating", and (Route B) the electrical "shape memory" effects (②→③) of ZIF-7@Cu-HHTP heterostructured ncs toward acetone under 5V (DC): the formation of *E*-meta state (③) to overcome the blocking effects of the electrical "gating".

Importantly, incorporating chemiresistive sensors allows the conversion of invisible electrical "shape memory" effects and metastable states to real-time visible electrical signals (resistance or current) with a high signal-to-noise level. This provides a novel and quantifiable technique for monitoring changes in the flexibility/softness of crystals ranging from the nanoscale to the microscale.

The wide applicability of our *c*MOF-on-*i*MOF design strategy has been demonstrated for various *i*MOFs. The seeded LbL method can be readily employed to grow *c*MOFs on 1D MOF-76(Tb) nanowires growing along the [001] direction (**Figures S48a** and **S49**) or 2D *i*MOFs (Kagomé (KGM) type KGM-OEt nanoflakes with dominant (001) facets, OEt=5-Ethoxyisophthalate, **Figures S48b** and **S49**).

Conclusion

In summary, we have demonstrated a seed-assisted synthesis method for constructing core-shell heterostructured nanocrystals (*c*MOF-on-*i*MOFs) consisting of redox-active *c*MOF-coatings on *i*MOFs with mismatched lattices. As a proof of concept, the porous interface created by hybridizing bonds between Zn, bim, Cu, and HHTP/HITP enabled the tuning of adsorption isotherms toward specific gases, affecting both the gate-opening pressure and sorption capacity. This tunability significantly enhanced the sorption selectivity. Interestingly, under direct electrical control, the transduced signals exhibited enhanced sensitivity and selective gate-opening behavior toward specific gas analytes in the corresponding chemiresistors. The structural transitions associated with visible electrical flexibility and unique electrical "shape memory" effects were revealed through *operando* GIWAXS imaging.

The ability to flexibly design the crystal structure of the MOF sheaths to achieve desired properties makes *c*MOF-on-*i*MOF heterostructures a promising candidate for designing materials with advanced gas handling capabilities. Furthermore, it provides a general approach for developing high-performance multifunctional materials for electrical devices such as batteries, supercapacitors, catalysis, and more.

Acknowledgments

This work was supported by the national natural science foundation of China (21801243), the KAKENHI Grant-in-Aid for Scientific Research (S) (JP18H05262, JP22H05005) and (C) (JP22K05128) from the Japan Society of the Promotion of Science (JSPS), and International Research Fellow of JSPS (Postdoctoral Fellowships for Research in Japan (Standard), P18334). Synchrotron X-ray measurements were supported by the Japan Synchrotron Radiation Research Institute (JASRI) (Proposal No. 2020A1628, 2020A1819, 2021A1542, 2021A1683, 2021B1886, 2021B1950). We thank the iCeMS analysis center for the access to the analytical instruments. We warmly thank Ms. M. Gochomori for her contributions to the ligand synthesis, as well as Renjun Zhang, Meng Wang, Haiyan Jiang and Jianze Xiao for the fruitful discussions and help with manuscript editing.

Keywords: metal-organic frameworks • conductivity • soft porosity • operando • shape memory

References

[1] a) G. Ferey, C. Mellot-Draznieks, C. Serre, F. Millange, J. Dutour, S. Surble, I. Margiolaki, *Science.* **2005**, *309*, 2040-2042; b) A. P. Katsoulidis, D. Antypov, G. F. Whitehead, E. J. Carrington, D. J. Adams, N. G. Berry, G. R. Darling, M. S. Dyer, M. J. Rosseinsky, *Nature* **2019**, *565*, 213-217; c) M. Kondo, T. Yoshitomi, H. Matsuzaka, S. Kitagawa, K. Seki, *Angew. Chem. Int. Ed.* **1997**, *36*, 1725-1727; d) K.-J. Chen, D. G. Madden, S. Mukherjee, T. Pham, K. A. Forrest, A. Kumar, B. Space, J. Kong, Q.-Y. Zhang, M. J. Zaworotko, *Science* **2019**, *366*, 241-246; e) S. Krause, V. Bon, I. Senkovska, U. Stoeck, D. Wallacher, D. M. Többens, S. Zander, R. S. Pillai, G. Maurin, F.-X. Coudert, S. Kaskel, *Nature* **2016**, *532*, 348-352; f) J. E. Mondloch, M. J. Katz, W. C. Isley Iii, P. Ghosh, P. Liao, W.

Bury, G. W. Wagner, M. G. Hall, J. B. DeCoste, G. W. Peterson, R. Q. Snurr, C. J. Cramer, J. T. Hupp, O. K. Farha, *Nat. Mater.* **2015**, *14*, 512-516; g) P.-Q. Liao, N.-Y. Huang, W.-X. Zhang, J.-P. Zhang, X.-M. Chen, *Science* **2017**, *356*, 1193-1196; h) M. D. Allendorf, R. Dong, X. Feng, S. Kaskel, D. Matoga, V. Stavila, *Chem. Rev.* **2020**, *120*, 8581-8640.

[2] S. Horike, S. Shimomura, S. Kitagawa, *Nat. Chem.* **2009**, *1*, 695-704.

[3] a) A. Ghoufi, K. Benhamed, L. Boukli-Hacene, G. Maurin, *ACS Central Sci.* **2017**, *3*, 394-398; b) A. L. Kolesnikov, Y. A. Budkov, J. Möllmer, M. G. Kiselev, R. Gläser, *J. Phys. Chem. C* **2019**, *123*, 10333-10338; c) J. P. Dürholt, B. F. Jahromi, R. Schmid, *ACS Central Sci.* **2019**, *5*, 1440-1448; d) K. Chen, R. Singh, J. Guo, Y. Guo, A. Zavabeti, Q. Gu, R. Q. Snurr, P. A. Webley, G. K. Li, *ACS Appl. Mater. Interfaces* **2022**, *14*, 13904-13913.

[4] a) S. B. Peh, A. Karmakar, D. Zhao, *Trends Chem.* **2020**, *2*, 199-213; b) C. Gu, N. Hosono, J.-J. Zheng, Y. Sato, S. Kusaka, S. Sakaki, S. Kitagawa, *Science* **2019**, *363*, 387-391; c) L. Li, R.-B. Lin, R. Krishna, H. Li, S. Xiang, H. Wu, J. Li, W. Zhou, B. Chen, *Science* **2018**, *362*, 443-446; d) Z. Meng, R. M. Stolz, L. Mendecki, K. A. Mirica, *Chem. Rev.* **2019**, *119*, 478-598; e) L. S. Xie, G. Skorupskii, M. Dinca, *Chem. Rev.* **2020**, *120*, 8536-8580.

[5] A. Knebel, B. Geppert, K. Volgmann, D. Kolokolov, A. Stepanov, J. Twiefel, P. Heitjans, D. Volkmer, J. Caro, *Science* **2017**, *358*, 347-351.

[6] a) S. Krause, N. Hosono, S. Kitagawa, *Angew. Chem. Int. Ed.* **2020**, *59*, 15325-15341; b) K. Ikigaki, K. Okada, Y. Tokudome, T. Toyao, P. Falcaro, C. J. Doonan, M. Takahashi, *Angew. Chem. Int. Ed.* **2019**, *58*, 6886-6890; c) M. S. Yao, J. W. Xiu, Q. Q. Huang, W. H. Li, W. W. Wu, A. Q. Wu, L. A. Cao, W. H. Deng, G. E. Wang, G. Xu, *Angew. Chem. Int. Ed.* **2019**, *58*, 14915-14919; d) C. Liu, Q. Sun, L. Lin, J. Wang, C. Zhang, C. Xia, T. Bao, J. Wan, R. Huang, J. Zou, *Nat. Commun.* **2020**, *11*, 4971; e) X. G. Wang, L. Xu, M. J. Li, X. Z. Zhang, *Angew. Chem. Int. Ed.* **2020**, *59*, 18078-18086; f) S. Bi, H. Banda, M. Chen, L. Niu, M. Chen, T. Wu, J. Wang, R. Wang, J. Feng, T. Chen, *Nat. Mater.* **2020**, *19*, 552-558.

[7] G. Lee, S. Lee, S. Oh, D. Kim, M. Oh, *J. Am. Chem. Soc.* **2020**, *142*, 3042-3049.

[8] a) Z. Wang, S. Wannapaiboon, K. Rodewald, M. Tu, B. Rieger, R. A. Fischer, *J. Mater. Chem. A* **2018**, *6*, 21295-21303; b) F. Wang, H. Wang, T. Li, *Nanoscale* **2019**, *11*, 2121-2125.

[9] a) S. Furukawa, K. Hirai, Y. Takashima, K. Nakagawa, M. Kondo, T. Tsuruoka, O. Sakata, S. Kitagawa, *Chem. Commun.* **2009**, 5097-5099; b) L. Feng, K.-Y. Wang, J. Powell, H.-C. Zhou, *Matter* **2019**, *1*, 801-824.

[10] O. Shekhah, H. Wang, D. Zacher, R. A. Fischer, C. Wöll, *Angew. Chem. Int. Ed.* **2009**, *48*, 5038-5041.

[11] M. Tu, C. Wiktor, C. Rösler, R. A. Fischer, *Chem. Commun.* **2014**, *50*, 13258-13260.

[12] M. G. Campbell, S. F. Liu, T. M. Swager, M. Dinca, *J. Am. Chem. Soc.* **2015**, *137*, 13780-13783.

[13] Y. Sakata, S. Furukawa, M. Kondo, K. Hirai, N. Horike, Y. Takashima, H. Uehara, N. Louvain, M. Meilikhov, T. Tsuruoka, *Science* **2013**, *339*, 193-196.

[14] N. Hosono, A. Terashima, S. Kusaka, R. Matsuda, S. Kitagawa, *Nat. Chem.* **2019**, *11*, 109-116.

[15] M. Kondo, S. Furukawa, K. Hirai, S. Kitagawa, *Angew. Chem. Int. Ed.* **2010**, *49*, 5327-5330.

[16] a) P. Zhao, H. Fang, S. Mukhopadhyay, A. Li, S. Rudić, I. J. McPherson, C. C. Tang, D. Fairen-Jimenez, S. E. Tsang, S. A. Redfern, *Nat. Commun.* **2019**, *10*, 999; b) Y. Du, B. Wooler, M. Nines, P. Kortunov, C. S. Paur, J. Zengel, S. C. Weston, P. I. Ravikovitch, *J. Am. Chem. Soc.* **2015**, *137*, 13603-13611.

[17] a) M.-S. Yao, W.-H. Li, G. Xu, *Coord. Chem. Rev.* **2021**, *426*, 213479; b) W.-T. Koo, J.-S. Jang, I.-D. Kim, *Chem* **2019**, *5*, 1938-1963.

[18] a) M. S. Yao, J. J. Zheng, A. Q. Wu, G. Xu, S. S. Nagarkar, G. Zhang, M. Tsujimoto, S. Sakaki, S. Horike, K. Otake, S. Kitagawa, *Angew. Chem. Int. Ed.* **2020**, *59*, 172-176; b) Y. Y. Jian, D. Y. Qu, L. H. Guo, Y. J. Zhu, C. Su, H. R. Feng, G. J. Zhang, J. Zhang, W. W. Wu, M. S. Yao, *Front. Chem. Sci. Eng.* **2021**, *15*, 505-517.

[19] M. A. Bañares, I. E. Wachs, *J. Raman Spectrosc.* **2002**, *33*, 359-380.